



Use of SBA-15 silica grains for engineering mixtures of oxides CoFe and NiFe for Advanced Oxidation Reactions under visible and NIR

Nabil Tabaja^{a,b,c}, Dalil Brouri^a, Sandra Casale^a, Sahar Zein^b, Mira Jaafar^b, Mohamed Selmane^d, Joumana Toufaily^{b,c,*}, Anne Davidson^a, Tayssir Hamieh^{b,c,*}

^a Sorbonne Universités, Université Pierre et Marie Curie, Laboratoire de Réactivité de Surface, UMR CNRS 7197, 4 Place Jussieu Tour 43-53 – 3^{ème} étage, 75252, Paris, France

^b Université Libanaise, Faculté des Sciences, Laboratoire de Matériaux, Catalyse, Environnement et Méthodes Analytiques, MCEMA, Hadath, Lebanon

^c Université Libanaise, École Doctorale en Sciences et Technologie, Laboratoire des Études Appliquées au Développement Durable et Énergie Renouvelable, LEADDER, Beyrouth, Lebanon

^d Sorbonne Universités, Institut des Matériaux de Paris Centre, case courrier 282, 4 place Jussieu, 75252, Paris, France

ARTICLE INFO

Keywords:

Nanoparticles
Spinel
Photocatalysis
Pesticides
Visible light

ABSTRACT

The fabrication of nanomaterials for specific applications, for plants protection and ameliorated production is an important and fast growing research field. In the present work, particularly small nanoparticles of several oxides were dispersed on SBA-15 silica mesoporous grains starting from metallic chlorides (Co, Ni, Fe). Samples were labelled NiFe_700_SBA-15 and CoFe_700_SBA-15, with 700 corresponding to the used calcination temperature. Characterizations were performed by X-ray fluorescence, XRD and TEM associated with EDS and SAED. Three main kinds of oxides were identified: 1) Co_3O_4 and NiFe_2O_4 bulk nanoparticles of structure close to magnetite (cubic, with one M(II) for two Fe(III) cations), 2) defect containing nanowires of CoFeO_3 , 3) $\text{Ni}_{0.5}\text{Fe}_{0.5}\text{O}$. UV–vis measurements were performed to demonstrate that the prepared mixtures were able to absorb light in the visible (and the NIR) spectral ranges. The developed NiFe_700_SBA-15 and CoFe_700_SBA-15 mixtures were successfully tested for the heterogeneous photocatalytic oxidation of a pesticide, carbendazim. In the used experimental conditions, an Aerioxide titania P25 reference (EVONIK®) was found poorly active only and the activity measured with CoFe_700_SBA-15 was better than the one of NiFe_700_SBA-15.

1. Introduction

Pesticides are large organic molecules used to control diseases in plants and fruits. In particular, banana, mango, strawberries, pineapples and apples, are heavily treated worldwide with pesticides, which now poses a salient ecological threat [1]. Carbendazim is strictly controlled in European countries. Carbendazim (MBC, methyl 1H-benzimidazol-2-ylcarbamate, $\text{C}_9\text{H}_9\text{N}_3\text{O}_2$) is a very active ingredient in itself and is also a product of decomposition of other fungicides of the broad benzimidazole family. Carbendazim is classified by the World Health Organization (WHO) as “likely to present risks in normal use” and is included in the group 2 of pesticides with potential long term effect on the PAN international List of Hazardous Pesticides [2,3]. MCB as a solid is not stable in aerobic conditions and is partially mineralized, transformed into CO_2 and water at 30–36% in 244–270 days [4]. Solid deposits remain then stable for a long time at 70–64% in soils, plants, or

fruits, as demonstrated recently with grape leaves [5].

It is now generally admitted that nanoparticles of oxides have properties that differ strongly from those of more conventional micron-sized particles [6]. In particular, activated electron transitions between their valence-electronic band, VB and their conduction band, CB can be obtained when they are irradiated with photons having the necessary energy, that is called band-gap. Intermediates that are called Reactive Oxygen Species, ROS, $\text{O}_2^{\cdot-}$, $\cdot\text{OH}$, $\text{H}_2\text{O}^{\cdot}$ are generated and can be involved in oxidation and reduction reactions of reagents. Ideally, these reactions can yield to a complete mineralization. Nanoparticles of the most studied oxide used in this research field, titania, can be prepared by several techniques, including sol-gel in water, with or without added polymers [7], in water and also in other solvents [8]. To introduce magnetic properties, another chemical element is necessary. Nanoparticles (NP) of magnetite, a Fe-containing oxide have been introduced and used for water depollution and also for biomedical applications, to

* Corresponding authors at: Université Libanaise, Faculté des Sciences, Laboratoire de Matériaux, Catalyse, Environnement et Méthodes Analytiques, MCEMA, Hadath, Lebanon.

E-mail addresses: joumana-toufaily@ul.edu.lb (J. Toufaily), anne.davidson@sorbonne-universite.fr (A. Davidson).

<https://doi.org/10.1016/j.apcatb.2019.04.073>

Received 21 February 2019; Received in revised form 18 April 2019; Accepted 21 April 2019

Available online 22 April 2019

0926-3373/ © 2019 Published by Elsevier B.V.

kill cancer cells by hyperthermia [9]. Ni and Co-ferrites of spinel structure are isolants, with a band-gap that can be activated by visible light. With added H_2O_2 , these NP surface can be used to produce reactive oxygen radicals for pollutant decomposition and also to kill living pathogens in water, such as fungi [10] and bacteria [11]. Several previous studies have addressed pesticides photocatalytic decomposition both in waste water and in rain water [12]. We have selected to work with catalysts working at low cost, using visible excitation lamps. In practice, in reported data, a small pollutant amount (ca 20 ppm) remains in water after reactivity tests, it is then still necessary to find active photocatalysts able to work at this important dilution level.

The present work describes the formation and stabilization of mixtures of oxide nanoparticles NiFe₇₀₀SBA-15 and CoFe₇₀₀SBA-15 dispersed on ordered mesoporous silica grains and submitted to calcination in air at 700 °C. An aerioxide titania commercial is introduced as a reference and the three samples are used to oxidize a pesticide, carbendazim, in diluted aqueous solution containing diluted O_2 species, at acidic pH. Since understanding the optical properties and the electronic structure of solids is important to improve their photocatalytic reactivity and also to develop new fields of application, their UV visible spectra have been collected and analyzed by a technique deriving from Tauc methodology. As well established for solids such as Si, with allowed direct electronic transitions (vertical electronic transition, K vector similar for fundamental and excited energy levels), a plot representing α , absorption coefficient multiplied by the photons energy in eV and a power 2, $(\alpha E)^2$, as function of E is expected to be a straight line. Its origin divided by its slope is giving the corresponding energy. For allowed but indirect electronic transitions, a lattice vibration is involved and a plot representing $(\alpha E)^{1/2}$ as a function of E is necessary [13]. For practical reasons, detailed in the results part, we have replaced α by F(R), Kubelka-Munk transformation of the signal recorded in reflectance. Photocatalytic reactivity was then experimentally evaluated for the decomposition of a low concentration (20 ppm, an amount that is standard for photo-catalytic tests) of a pesticide, carbendazim, in water, in air and under a halogen (visible + NIR) light. Quantifications in solution have been made by High Performance Liquid Chromatography, HPLC. The obtained results compare favorably with previous literature reports about new photocatalysts for carbendazim elimination in the NIR spectral range [14].

2. Experimental part

2.1. Materials

Reagents were all provided by Sigma Aldrich. Tetraethyl orthosilicate, reagent grade 98 in weight %; poly-block (oxyethylene) - block-poly (oxypropylene) - block-poly (oxyethylene) triblock copolymer Pluronic, P123, of molecular weight 5800 g. mol⁻¹. They were used as received, no pretreatment. The precipitation of a hybrid organic-inorganic material was obtained in an HCl aqueous solution, of concentration 0.3 mol. L⁻¹, prepared starting from a commercial acidic solution at 35% in volume from Carlo Erba. FeCl₃, NiCl₂ and CoCl₂ were provided by Sigma Aldrich and were selected for their ACS grad.

Table 1
Summary of textural properties measured by N₂ sorption at 77K.

| Sample | V _p ^a (cm ³ .g ⁻¹) | Microporous volume(cm ³ .g ⁻¹) | S _{BET} ^b (m ² .g ⁻¹) | ΔS(m ² .g ⁻¹) | D _{pore} ^c (nm) |
|---------------------|---|---|--|--------------------------------------|-------------------------------------|
| SBA-15 | 1.40 | 0.90 | 741 | | 8.2 |
| CoFe ₇₀₀ | 1.05 | 0.03 | 574 | −167 | 6.6 |
| NiFe ₇₀₀ | 1.05 | – | 554 | −187 | 6.5 |

^a Porous volume, single point determined at P/P° 0.98. ΔV/V_p, 25% of decrease after metal deposition and calcination. 75% preserved.

^b Specific surface area, determined within the P/P° range 0.05–0.30, as recommended for mesoporous samples.

^c Mesopore diameter calculated on the desorption branch of the isotherm.

2.2. Mesoporous silica preparation

A single batch of SBA-15 silica was prepared under the conditions described by Sayari et al. [16] and by scaling up the reagent proportions to obtain more than 50 g of calcined silica [17]. 1319 mL of distilled water were acidified with 35.5 mL of HCl (35 vol. %), and then 71.61 g of P₁₂₃ was added. The temperature of the reactor was set at 35 °C. Then, 168 mL of TEOS were added drop wise, at a rate of 2 mL.min⁻¹, using a turbo-pump (Gilson). Stirring was set at 160 rpm and stopped directly at the end of the addition of TEOS. Precipitation occurred at 35 °C, for 24 h, in static conditions (beaker open to let evaporate the alcohol formed by TEOS hydrolysis and condensation). 400 mL of liquor with precipitated white silica grains in suspension were transferred for maturation at 35 °C during 65 h into an autoclave. A hydrothermal treatment at 130 °C for 33 h was finally applied. Silica was recovered by filtration and washed with distilled water (3 L) to eliminate, as much as possible, chlorine contamination. The powder was dried for 24 h in air at room temperature, then calcined in air at 2 °C.min⁻¹ up to 500 °C, and kept at this temperature for 6 h. After cooling down of the oven, the calcined silica was recovered between 200 and 150 °C and stored in closed vials to avoid contact with moisture and air before Co, Ni and Fe-loading.

2.3. Dispersion of metallic species on silica and calcination

For each preparation, two solvents were introduced, water and cyclohexane and the 2S technique [18,19] was used. 1 g of calcined silica was suspended in 75 mL of cyclohexane. Then, an aqueous solution of the chloride iron salt and of a divalent metallic M (M = Ni, Co) chloride was added drop-by-drop. The volume and concentration of the added aqueous solutions were calculated to obtain the desired percentage in weight of metal (% Fe + % M = 10–12 weight, wt%). The addition of the aqueous solution was fast (less than 5 min) and a simple decantation was then sufficient to separate the remaining solid and the organic solvent. The recovered powder which contains the aqueous solution of metallic salts was left to dry in air, at room temperature, for at least 12 h, to remove the remaining solvent and to avoid any further auto-combustion reaction between nitrate anions and organic molecules. Calcination at 700 °C at a rate of 2 °C.min⁻¹ in a muffle furnace and in air was then performed to transform the precursor(s) salt(s) into oxides and metallic silicates. At the end of the calcination step, the samples were quenched to room temperature. Preparation conditions and chemical analysis results are summarized in Table 1.

2.4. Characterization techniques

Chemical analysis of the prepared samples was made with an XEPOS XRF apparatus (SPECTRO). Samples were analyzed in their powder form and quantitative data were determined by using the Micro Powder software.

Specific surface areas, pore volumes, diameters of the main pores were measured by N₂ sorption with an ASAP 2020 apparatus (Micromeritics). Specific surface areas were calculated from the analysis of the relative pressure range (0.05–0.25) using the Brünauer-

Emmett-Teller (BET) method [20]. The overall pore volume was measured from a single point at a relative pressure $P/P^\circ = 0.98$, and the pore size was determined by Barrett-Joyner-Halenda (BJH) method applied to the desorption branch of the isotherm. t-plots were also drawn to obtain microporous volumes.

TEM micrographs offered unique advantages, the possibility to study a solid with a resolution which can be as small as 2 Å and to obtain local compositions and diffraction results on specific kinds of nanoparticles. We have used a microscope JEOL JEM 2011 operating at 200 kV. Calcined catalytic powders were suspended in ethanol and dried on carbon-coated copper grids. Identified well-crystalline domains, characterized by long and parallel clear and dark stripes, have been observed. On these specific objects, we have used measurements of characteristic distances between dark stripes, as well as a mathematical treatment by Fourier transformation. Electrons are coherently scattered (diffracted) by the lattice of well-ordered solids, multiples nanoparticles without commun ordering are giving concentric rings. If a large enough crystalline nanoparticle is selected, a diffracted spot is generated for each h^*k^*l node of the reciprocal lattice, with h , k and l Miller indices. In XRD, the same three indices are used to identify families of crystallographic reticular parallel planes. To investigate the location of replicated oxides nanoparticles either outside silica grains or inside pores, we have used ultrathin sections (70 nm thickness). These sections were prepared as follows: a few milligrams of the sample powder were mixed with EPON 812 embedding resin in a Beam capsule. Polymerization of the mixture took place at 60 °C during 48 h. The polymerized blocks were cut with a diamond knife in ultrathin sections which were deposited on TEM grids. Images were recorded with a resolution of 1.8 Å. Electron Diffusion X-ray Spectroscopy was used to obtain atomic ratios in Co, Ni, Fe, Cl (if traces), Si (if there is a superposition of nanoparticles or a silicon-doping).

An ADVANCE D8 Bruker diffractometer with a Bragg-Brentano geometry working at 40 kV and 30 mA and working at Cu K α wavelength (average λ of the doublet, 1.5418 Å) was used. A precise Lynx Eye detector was used. Diffractions reported here were recorded in the $5 < 2\theta < 90^\circ$ range. Crystalline phases were identified, mostly by using the FullProf software and by direct comparison with files in ICDD database (The International Center for Diffraction Data). Peak positions and full widths at half-maxima (FWHM) were obtained. The software also evaluates an average value of coherent domain sizes. We took into account reported unit-cell parameters of 8.04 Å for Co₃O₄ (ICDD 071-4921), 8.35 Å for maghemite γ -Fe₂O₃ (ICDD 71-6336), 8.15 Å for Co₃O₄ (ICDD 71-4921) for a spinel structure, i.e. a cubic unit-cell, belonging to the Fd-3 m group of symmetry.

A Cary 5000 spectrometer (Varian) was used to record UV-vis-NIR spectra, in the 200–2500 nm spectral range, in air and at room temperature. This apparatus is equipped with a diffuse reflectance internal cell (70 mm diameter) covered with Teflon® (polytetrafluoroethylene) which was used as a blank for baseline measurements. Spectra were collected with a split broad width (SBW) of 2 nm and a rate of 600 nm per min.

2.5. Absorption and elimination of Carbendazim (MBC)

One halogen lamp (100 W RJH-TD Radium) emitting both in the visible and in the NIR range, was placed directly inside a closed glass tube inserted in a double-walled cylindrical reactor. An aqueous solution of 20.00 ± 0.04 ppm of CBM in distilled water was prepared. 98 mL of this solution were introduced into the photochemical reactor and then 75 mg of solid catalyst was dispersed inside. The pH of reaction was adjusted to 2.6 by adding a few drops of an aqueous H₂SO₄ solution, at a concentration of 1 mol. L⁻¹. The reactor was placed into a black box and thermalized with a (16 L) water bath. The temperature was set at 35 °C and the system was left to equilibrate during 30 min. 2 mL of 30 wt% H₂O₂ solution was added and the halogen lamp was turned on. Aliquots were taken at different reaction times (3, 5, 10, 15,

30, 60, 120, 180, 240, and 300 min) with a 1 mL syringe fitted with a 15 cm needle and 0.2 μ m filters. CBM concentration was measured as a function of time with an HPLC-DAD apparatus equipped with a Thermo-ODS C₁₈ Hypersil column (5 mm diameter, 4.6*250 mm) and a UV detector. The flow-rate of the elution solvent (methanol/water; 40:60 in volume %) was set at 1 mL.min⁻¹ and the injected volume was 20 μ L. This method was previously used and optimized for the quantification of carbendazim in water [21]. To allow comparison with the titania Aeroxide EVONIK® activity, the same lamp was used and also a UV mercury lamp, of intensity 10⁻⁵ Einstein.L⁻¹. s⁻¹.

2.6. Iron leaching measurements

Fe(II) species are generated by leaching. We were expecting their complete oxidation into Fe(III) and measured the Fe(III) concentration after 1400 min of catalytic test and 24 h of storage at low temperature by a colorimetric method using a complexation reaction, selected among possible spectrophotometric reagents [22]. Aqueous solution containing Fe(III) ions was reacted with an aqueous solution containing KSCN and then cyanide anions (SCN⁻) to form a Fe (SCN)²⁺ bright red complex with an absorbance maximum at 475 nm. In practice, after 1400 min of reaction, the remaining solid and solution were separated by centrifugation (7000 rpm, 15 min) and the solution was recovered. This solution was filtered using a syringe with a filter (0.2 μ m pore diameter) to eliminate as much as possible traces of small NP and remaining colloids in the reaction medium. Then, 10 mL of the solution were placed in a beaker and 1 mL of a solution of potassium cyanide of concentration 200 g. L⁻¹ was added. The complex was quantified by its absorbance at 475 nm with a UV-vis 6715, JENWAY apparatus. The concentration was calculated by introducing the Beer-Lambert law and a calibration line obtained with six reference solutions (regression coefficient, χ^2 larger than 0.987).

3. Results and discussion

3.1. Porous architecture

Fig. 1 displays N₂ absorption isotherms of SBA-15 calcined silica and of Co, Fe-loaded (CoFe_700) and Ni, Fe-loaded (NiFe_700) samples. The three powders were calcined at 700 °C, in air and at 2 °C min then quenched. The three isotherms are of type IV and associated with an H1 hysteresis in IUPAC classification [20]. As summarized in Table 1, micropores, detected by the vertical high position of the first horizontal line, from 0.30 to the beginning of the hysteresis on blank silica (blue curve) are less detected for the NiFe_700 (red) and CoFe_700 (black).

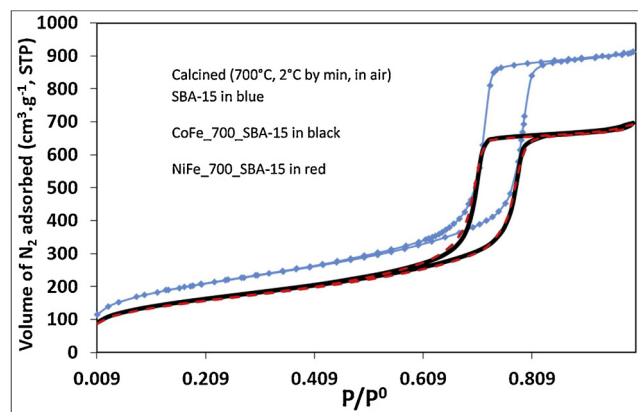


Fig. 1. N₂ sorption results as obtained on blank silica calcined at 700 °C and on NiFe₇₀₀SBA-15 (red) and CoFe₇₀₀SBA-15 (black). Heating rate of 2 °C. min⁻¹ and quenching (For interpretation of the references to colour in this figure legend, the reader is referred to the web version of this article.).

Table 2

Comparison of chemical composition obtained by located EDS (n_{Co} and n_{Ni}) and by X-ray fluorescence. 1_Co and 1_Ni EDS are expressed in weight (wt) and in atomic percentages, X-ray fluorescence are in wt%.

| CoFe_700 | | | | | NiFe_700 | | | | | | | | |
|----------|------|-------|----------|----|----------|------|------|------|------|------|------|------|----------|
| 1_Co | | 2_Co | XRF | | 1_Ni | | 2_Ni | 3_Ni | 4_Ni | 5_Ni | 6_Ni | 7_Ni | XRF |
| at. % | wt % | at. % | Cl: 0.00 | | at. % | wt % | At % | | | | | | Cl: 0.05 |
| O | 61.3 | 31.8 | 56.3 | | 61.3 | 31.1 | 51.3 | 19.7 | 15.9 | 49.1 | 47.3 | 29.3 | |
| Fe | 18.4 | 33.3 | 20.2 | 5 | 22.9 | 40.6 | 22.3 | 39.0 | 48.8 | 3.1 | 2.3 | 42.2 | 6 |
| Co | 16.2 | 31.0 | 20.9 | 5 | 0.0 | 0.0 | 0.0 | 0.0 | 0.1 | 0.0 | 0.0 | 0.3 | |
| Ni | 0.1 | 0.2 | 0.1 | | 14.6 | 27.2 | 24.5 | 29.9 | 30.0 | 45.6 | 46.2 | 24.4 | 7 |
| Si | 4.0 | 3.6 | 2.5 | 40 | 1.2 | 1.1 | 1.9 | 11.3 | 5.1 | 2.2 | 4.2 | 3.8 | 38 |
| M/Fe | 0.9 | | 1.0 | | 0.6 | | 1.1 | 0.8 | 0.6 | 0.9 | 1.0 | 0.6 | |

Only a part of the mesoporous volume remains accessible, after metal deposition and calcination. With the two metals containing samples, the total porous volume was affected (decreased by 25%, 75% remaining open and accessible). The diameter of the main mesopores is decreased.

Table 2 displays chemical compositions obtained by X-ray fluorescence (for Si, Cl, Fe, Co, Ni in weight %) compared to EDS measurements. The atomic number of oxygen, $Z_{\text{O}} < 12$, was too small to allow its detection with the used equipment. Similar Fe and M values are obtained for Fe and Co species in CoFe_700, respectively 48,880 and 49,500 mg kg. A small chloride Cl contamination was remaining inside our silica precipitated powder and is not fully eliminated even after two calcinations (a first one performed in air at 500 °C to remove the organic surfactants from silica and a second one at 700 °C after deposition of metallic species). More localized EDS results, expressed as atomic %, and concerning independent nanoparticles, will be analyzed in a next independent paragraph. This method is much more sensitive and indicates that the prepared calcined solid contain nanoparticles that are slightly polluted, the CoFe_700 indeed contains $0.15 \pm 0.01\%$ of Ni and 4 to 2.5% of Si. A careful examination of the micrographs associated with these values is important since Si atoms are possibly detected by transparency (the superposition of several objects).

Precisions in wt (%) as determined by X-ray Fluorescence differ for several element, but it is not larger than ± 1.4 . X-ray fluorescence measurements were particularly important to complement EDS results before potential applications since no remaining chlorine contamination was detected in calcined CoFe_700_SBA-15, compared to 0.05 for NiFe_700_SBA-15

3.2. Metallic oxide nanoparticles located outside the silica grains

Mossbauer measurements have shown that very small clusters, characterized by a superparamagnetic behavior were present inside our calcined silica grains and can represent more than 40% of the introduced Fe-species. We have synthesized reference samples only containing these diluted species to characterize them. The analyzed further results only concern the very crystalline and external oxide nanoparticles that we have identified outside the silica grains.

Fig. 2 displays TEM micrographs measured on NiFe_700_SBA-15 and CoFe_700_SBA-15. Two main kinds of external metallic oxide nanoparticles were observed, in deep grey on almost white silica grains. Symbols (a) and (b) have been added in Fig. 2 to distinguish two types of nanoparticles. The (a) symbol is introduced circa very small nanoparticles, with clearly anisotropic shapes (nanowires, less than 10 nm diameter, average length circa 200 nm) and the (b) symbol circa larger ones (present in NiFe_700_SBA-15, apparent dimensions larger than 20 nm). The elongated aspect of the first kind of nanoparticles are described in the enlargement presented in Fig. 3A. The shapes of the larger nanoparticles are shown in Fig. 3B.

To inspect closely chemical compositions of oxide nanoparticles, EDS spectra measured with 200 kV TEM microscope were necessary

since on a given sample, nanoparticles with different shapes can be observed. The location and the size (blue circle) of measurements made by EDS on NiFe_700_SBA-15 in Fig. 3A on a nanowire and on Fig. 3B on bulkier kind of nanoparticles. The corresponding Fe, Ni, Si and O atomic % are given in Table 2. These measurements are labelled n_{M} with and M: Nickel and n a number to differentiate them. On Fig. 4, two selected micrographs specifically measured on nanowires in CoFe_700, spots of the region analyzed by EDS are also presented (blue circles). The corresponding spectra are presented on the right part of Fig. 4 and corresponding Fe, Co, Si and O atomic % are given in Table 2. CoFe_700 is slightly polluted in Ni (less than 0.1%) and the NiFe_700_SBA-15 in Co (0.3% but on one EDS measurement, only. 1_Co and 2_Co were measured on nanowires present in the CoFe_700_SBA-15 sample. They are characterized by an average Co/Fe ratio of 0.9 ± 0.1 and have a heterogeneous chemical composition as demonstrated by differences in Fe proportion between them (respective Fe values 18.4 and 20.2%). A Co/Fe atomic ratio close to 1 hampers an attribution to spinel CoFe_2O_4 and/or to Co_3O_4 . To go further and understand that point, we need the information given by XRD and by UV–vis spectroscopy. In NiFe_700 nanowires correspond to an atomic Ni/Fe ratio close to 2. They have a heterogeneous character, as demonstrated by differences between atomic percentages 3_Ni and 4_Ni respectively taken in the middle and at the end of a nanowire. An average Ni/Fe atomic ratio close to 0.7 ± 0.1 . All these measurements are associated with a large oxygen value. 3_Ni also corresponds an important atomic Si % pollution. An approximate NiFe_2O_4 chemical formula can be proposed. Other nanoparticles, studied in 2_Ni for instance (Fig. 3B) rather correspond to a possible $\text{Ni}_{0.5}\text{Fe}_{0.5}\text{O}$ chemical formula (with Si traces).

TEM micrographies measured on CoFe_700_SBA-15 are presented in Fig. 4.

In Fig. 4a, an additional red parallelogram indicated the region that was enlarged in Fig. 5A. Additional HR-TEM selected images on which reticular distances on monocrystalline domains were selected (Fig. 5A at the end of a nanowire of CoFe_700_SBA-15, red square on Fig. 4A; Fig. 5B: in a nanowire of NiFe_700_SBA-15 (not shown)). Alternating dark and clear stripes are observed. Distances between 10 dark lines, divided by 10, correspond to a reticular distance. Complements are measured after Fourier Transformation of the image. On these Fourier transformed images, interactions between electron signal and the ordered atoms of the 3D structure of the studied oxide was observed. The distance between pairs of symmetrical spots were measured with the ImageJ program and converted into distances. The measured distances were then associated with reticular planes, as indicated on the ICDD files used for the analysis of X-ray Diffraction measurements.

With the two solids presented in Fig. 5, an attribution of the largest measured distance to the 111 family of reticular planes inside spinel unit-cells can be proposed.

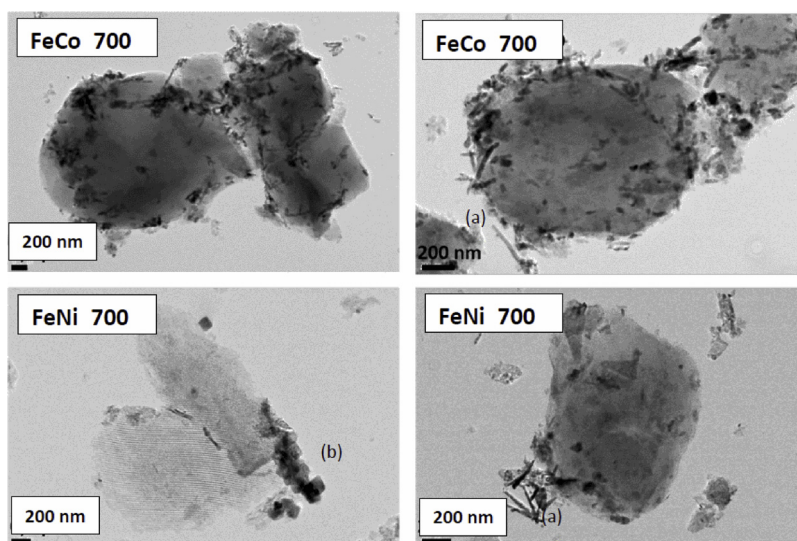


Fig. 2. TEM micrographs recorded on FeCo_700 (top) and FeNi_700 samples (bottom); (a) and (b) symbols added to discriminate nanowires and bulkier nanoparticles.

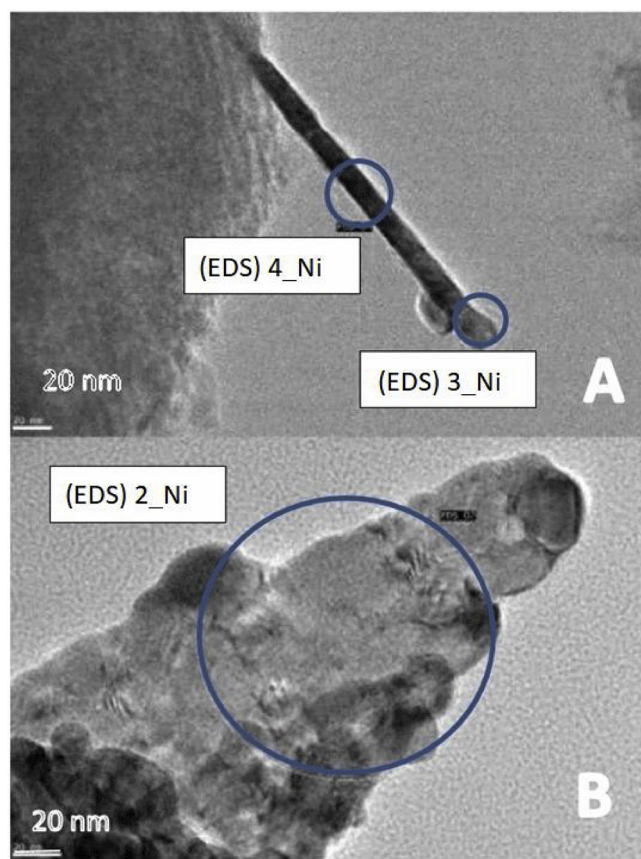


Fig. 3. TEM micrographs of two kinds of nanoparticles identified in NiFe_700_SBA-15: (A) a nanowire enriched in Fe and Ni also containing some Si pollution, middle (EDS) 4_Ni and extremity (EDS) 3_Ni, atomic ratios Fe/Ni = 0.61 and 0.77 and atomic % of Si species 5 and 12%, (B) an aggregate of bulkier nanoparticles, with identical Ni and Fe atomic %.

3.3. Structure of crystalline nanoparticles by XRD

X-ray diffraction measurements as obtained for (a) NiFe_700_SBA-15 and (b) CoFe_700 in Fig. 6 (A) and the simulation treatment made for CoFe_700_SBA-15 were presented in Fig. 6. Traces of hydroxides,

generated by corrosion are not introduced. Several position of cations can be expected with Co, Fe and Ni ions. Octahedral and tetrahedral cationic sites are possible for a given chemical composition MFe_2O_4 (1 M(II) and two Fe(III)) with M(II). In direct spinel, the M(II) are all located in Td sites. In inverse spinel, they are located in octahedral sites. Partial degree of inversion are also possible. Mixtures of oxides containing Fe (III) and M (II) species can keep a spinel cubic unit-cell and will give very similar diffractions, as observed for maghemite γ - Fe_2O_3 and magnetite Fe_3O_4 with pure Fe-oxides. The existence of a defect containing mineral $CoFeO_3$ is well-known. Recently, this phase has been studied for the exchange of its ions with Mn^{2+} and Nd^{3+} ions [23].

Fig. 6 (B) (a) and Fig. 6 (A) (a) are both relative to CoFe_700_SBA-15 and present this sample diffraction data without and after subtraction of an X-ray fluorescence background. Such a background was expected with a diffractometer using a copper anti-cathode. A first phase having a spinel cubic structure, is modelled using the FullProf program [13]. A a unit cell parameter of $8.387 \pm 0.004 \text{ \AA}$ and a particle size of $10.6 \pm 0.8 \text{ nm}$ are obtained for a space group Fd-3 m and a quality of simulation indicated by a χ^2 factor of 2.60 (reasonably close to 1 with the broad diffractions observed here on nanoparticles of small sizes). In that figure, measured points are in red, simulation in black. The green lines are relative to the positions of Bragg diffractions of $CoFeO_3$. A second crystalline phase is present. Indeed, other diffraction peaks are detected with positive intensities in the subtraction that is shown in blue in Fig. 6 (B). The blue curve is obtained by plotting the difference between observed values Y_{observed} and calculated ones $Y_{\text{calculated}}$, as a function of 2θ . The positions of the main positive diffraction peaks are observed at 31.1 , 36.7 , 44.6 and 59.1° and the four positions correspond quite well with the diffractions (220), (311), (400) and (511) of a second cubic phase, still with a spinel structure, probably Co_3O_4 (ICDD 42-1467).

All the diffraction peaks observed on the X-ray diffraction of the NiFe_700_SBA-15 sample in Fig. 6 (A) (b) can be associated also with a spinel phase, still in the Fd-3 m space group. A unit cell a parameter of $8.358 \pm 0.002 \text{ \AA}$, smaller than the one measured on the phase that we have identified as $CoFeO_3$ and an average coherent domain size of $7.8 \pm 0.4 \text{ nm}$, smaller than the one measured in TEM, are measured as expected for multi coherent-domains. The observed diffraction peaks of this phase are very close to the one of either γ - Fe_2O_3 or $NiFe_2O_4$ (ICDD 80-0072). Since the atomic Ni/Fe ratio in EDS was close to 0.5 for 1_Ni, 4_Ni and 7_Ni (average value of 0.61 ± 0.03), a chemical composition close to $NiFe_2O_4$ is possible. EDS measurements 2_Ni, 5_Ni, 6_Ni and

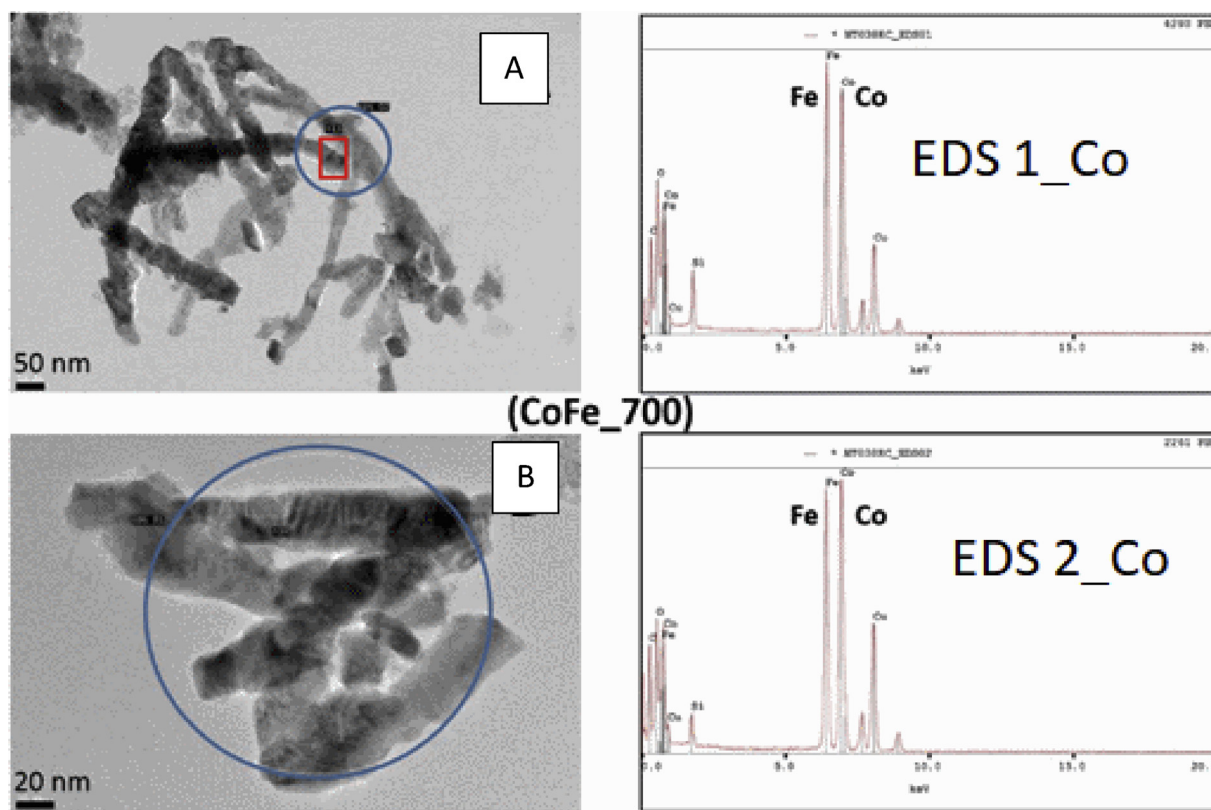


Fig. 4. TEM micrographs and EDS measurements of CoFe₇₀₀SBA-15, **A, B**) size and location of the two spots, blue circles, with atomic % values in Fe, Co, Si and O elements summarized as 1_Co and 2_Co in Table 2; **c, d**) EDS spectra 1_Co and 2_Co (For interpretation of the references to colour in this figure legend, the reader is referred to the web version of this article.).

3_Ni gave an average Ni/Fe ratio of 0.94 ± 0.09 suggesting that another crystalline phase is present. In XRD, the presence of this second phase could be proposed because the intensity of the (400) diffraction observed circa 43.5° is too important to associate it only with a pure NiFe₂O₄ phase. The detection of a too large intensity in that position rather suggests that another crystalline phase is present, possibly the mixed Ni_{0.5}Fe_{0.5}O phase or rather Ni_{0.5}Fe_{0.5}Si_{0.5}O was detected in Fig. 3 (since a variable u pollution in Si species was detected by EDS). A main diffraction circa 43.5° can be expected for this phase and will be superimposed on the (400) diffraction of the spinel NiFe₂O₄. Mixed Ni and iron phases were already described, for instance in Nickel-stainless steel alloys corroded in water, and in basic conditions at a high enough temperature [24]. The chemical composition of the used stainless steel was extremely complex as it contained C, S, P, Mn, Ni, Cr, Fe and Mo species and among these species, the Mn-ones were supposed to be responsible for an improved and good stability.

XRD (global) and EDS (local) were complementary and have shown that NiFe₇₀₀SBA-15 and CoFe₇₀₀SBA-15 samples were mixtures of several oxides. CoFe₇₀₀SBA-15 contained spinel nanowires having a

CoFeO₃ chemical composition. Another inorganic phase with a spinel structure was detected by XRD, Co₃O₄. The NiFe₇₀₀SBA-15 contains NiFe₂O₄ and several other oxides, in particular one having a Ni/Fe atomic ratio of 1 and to a low atomic oxygen percentage in EDS that corresponds to nanoparticles bulkier than the spinel nanowires in TEM. Furthermore, the observed diffraction peaks were broad as expected for nanoparticles and the quality of the two recorded X-ray diffraction was not resolved enough to allow a complete Rietveld analysis, in particular an accurate location of the inorganic cations. Methods to correct this point will be described in the conclusion part.

3.4. Spectroscopic additional information

In the UV visible spectral range, in addition to the band gap of oxide nanoparticles, intra-metallic M (d-d) transitions and intermetallic M-M' transitions (mediated by oxygen atoms) as well as Ligand to Metal, L to M (charge transfer positions) were detected. The respective size of cations in high spin are similar (Co(II): 0.72 pm, Ni(II): 0.74 pm; Fe(III): 0.79 pm, R.D. Shannon [25]). CoFe₂O₄ and NiFe₂O₄ are isolant and the

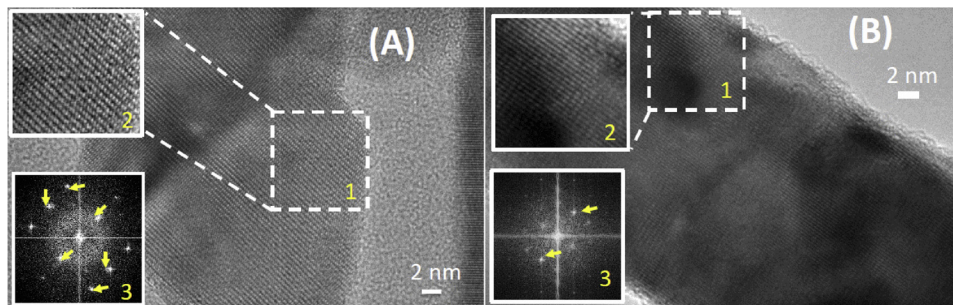


Fig. 5. HR-TEM of CoFe₇₀₀ (A) and NiFe₇₀₀ (B). 1: selected studied nanoparticles, 2: enlargement, 3: Fourier Transform. Arrows to indicate pairs of spots corresponding to a given h^*k^*l node in the reciprocal lattice and a hkl reticular plane in X-Ray diffraction. Measured distances of 0.46, 0.22 and 0.21 nm for CoFe₇₀₀SBA-15, 0.22 nm \pm 0.02 nm for NiFe₇₀₀SBA-15. Treatment by ImageJ program.

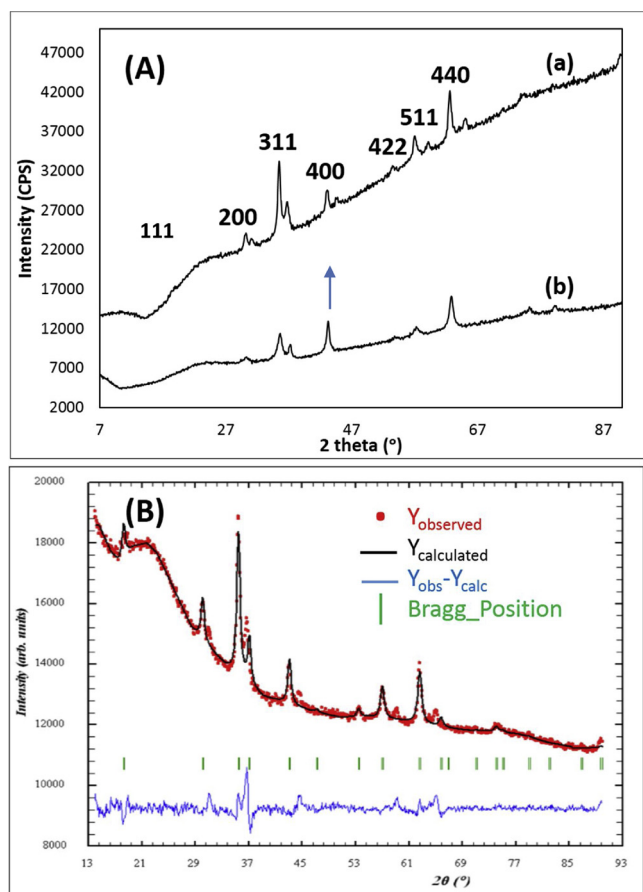


Fig. 6. Information by X-Ray diffraction. (A) X-ray diffraction measurements of: (a) CoFe₇₀₀SBA-15 with reticular planes identified by hkl Miller indexes, and (b) NiFe₇₀₀SBA-15, with a blue arrow indicating the (400) diffraction of spinel, too intense. (B) Treatment of the diffraction of CoFe₇₀₀ with the FullProf program. In red, diffraction points after subtracting a background due to X-ray fluorescence. In black simulation with FullProf. Y_{observed} values were the observed intensities, $Y_{\text{calculated}}$ the calculated ones and the blue curve was obtained by subtraction ($Y_{\text{observed}} - Y_{\text{calculated}}$). Green lines were indicating the positions of the diffraction peaks of Co₃O₄ with a spinel structure in ICDD 071-4921.

(A) X-ray diffraction measurements of: (a) CoFe₇₀₀SBA-15 with reticular planes identified by hkl Miller indexes, and (b) NiFe₇₀₀SBA-15, with a blue arrow indicating the (400) diffraction of spinel, too intense. (B) Treatment of the diffraction of CoFe₇₀₀ with the FullProf program. In red, diffraction points after subtracting a background due to X-ray fluorescence. In black simulation with FullProf. Y_{observed} values were the observed intensities, $Y_{\text{calculated}}$ the calculated ones and the blue curve was obtained by subtraction ($Y_{\text{observed}} - Y_{\text{calculated}}$). Green lines were indicating the positions of the diffraction peaks of Co₃O₄ with a spinel structure in ICDD 071-4921.

absorptions that are detected with these oxide solids can be well described using the electronic energy levels located on atoms. We have used the crystal field model, for which the Fe(III) ions of electronic configuration can be written with Argon, [Ar], introduced for 18 electrons, [Ar] 3d⁵ have no preference for Oh or Td sites. With its 5 electrons and because of the high spin situation is in general observed with cations in octahedral sites, with one unpaired electron by orbital, the energy of stabilization due to the crystal field is indeed the same and equal to zero in octahedral and in tetrahedral sites. No electronic transition due to an excitation of Fe(III) is expected to be seen. All the detected absorptions in the visible and NIR will be due to Ni(II) or Co(II) ions of respective electronic configurations, [Ar] 3d⁸ and [Ar] 3d⁷.

The spectrum of NiFe₇₀₀SBA-15 has been measured in reflectance and in air. Three main peaks corresponding to a main location of Ni(II)

ions in Oh sites were observed. With the electronic configuration of Ni(II) in an Oh symmetry, a fundamental ³A_{2g} energy level is calculated and the three absorption peaks can be attributed to (d-d) electronic transitions: ν_1 : ³A_{2g} → ³T_{2g}, ν_2 : ³A_{2g} → ³T_{1g} (P) and ν_3 : ³A_{1g} → ³T_{1g} (F). The three experimental values are 1040, 750 and 395 nm. The octahedral crystal field parameter, Dq, can be calculated from the relation $10 \cdot Dq = 1/\nu_1$. The obtained value of 8425 cm⁻¹ is close to the one reported for symmetrical [Ni(II)(H₂O)₆]²⁺ hexaaquanickel (II) ion and for anisotropic forms appearing upon dehydration for Ni(II) ions grafted, attached by O-species to the surface of Y-zeolites [26]. Two other broad and overlapping absorptions are observed at 600 and 500 nm and confirmed that some Ni(II) ions occupy tetrahedral sites. NiFe₂O₄ has then a partially inverted spinel unit-cell and this level of structural determination was not accessible with the XRD presented here, too noisy. Possible corrections will be described in the conclusion section.

Less noisy data were obtained with the sample CoFe₇₀₀SBA-15. The obtained spectrum has been used to ascertain this solid ability to absorb in the visible spectral range through direct (electron excitation from fundamental to excited levels, by a photon) and/or an indirect electronic transitions (requiring an associated lattice participation, by a photon associated with a phonon). The UV-vis spectrum, recorded in reflectance, R% was converted into F(R) using the Kubelka-Munk formula, $F(R) = (1 - R_{\infty}^2)/2R_{\infty}$. We used F(R) rather than α , coefficient of absorption, because a precise thickness of light penetration is uneasy to evaluate with the present mixtures. By contrast, light reflection can be assumed to be completed and F(R) equal to F(R_∞). Indeed, no light lost can take place with the used sample holders and we have used an important thickness of powder experimentally (3–4 mm). We have assumed that the collected reflectance was sufficiently accurate for a semi-opaque powder, dark powder being used with an important dilution inside a white powder (11.6 mg of powder for 276 mg of Teflon®) and a carefully homogenized powder. We have then followed recommendations for accurate quantification of F(R) given in Ref. [27]. We have then plotted $[F(R) \times E]^2$ and $[F(R) \times E]^{1/2}$ as a function of the energy E (expressed in eV). The spectral range within 0.5 and 3.0 eV has been simulated using three straight lines which intercept the energy axis for both $n = 1/2$ and $n = 2$ coefficients. The first detected electronic transition is typically "located", direct and corresponds to some (d-d) electronic transitions. Its right part is masked by vibrations due to water and silanol groups. An energy value of 0.688 ± 0.027 eV was measured in its left part. This transition was spin-allowed but forbidden by symmetry rules. Its observation implied local structural distortions, in particular hybridization between metallic 3d and oxygen 2p orbitals. A similar energy value (0.75 eV) has been reported using the same technique, i.e., a plot of $[F(R) \times E]^2$ as a function of energy for CoFe₂O₄ vs NiFe₂O₄ thin films [28]. A value of 0.82 eV has also been reported with accurate and modern measurements performed on metal to oxides (CoO-Co₃O₄) thermal transformations studied by near-ambient pressure ultraviolet photoelectron spectroscopy (NAP-UPS) on a synchrotron [29]. In this recent publication, the hybridization of O 2p and Co 3d orbitals was demonstrated. For the second and third electronic transitions, we have selected between a direct and an indirect electronic transition by choosing the best linear coefficient, closest to 1, and by comparison with reported data, in particular the ones associated with electronic structure calculations based on Vienna Ab initio simulation package, VASP [30]. The second and third transitions were observed here at 1.09 (indirect) and 2.60 eV (direct). An indirect value at 2.7 eV was given in Ref. [30]. A value of 2.76 eV was reported in Ref. [28]. The two electronic transitions are, in general, associated with Co³⁺ in Oh sites, Co²⁺ to Co³⁺ charge transfer, to O 2p Co²⁺ or O 2p Co³⁺ electronic transitions.

The energy in J is calculated by dividing h ($h/2\pi = 1.054 \cdot 10^{-34}$ J.s⁻¹, Planck constant) multiplied by c ($3 \cdot 10^8$ m.s⁻¹, celerity of light in vacuum) by the wavelength measured in nm and multiplied by 10^{-9} (to obtain meters). Division by $1.602 \cdot 10^{-19}$ is necessary to convert J in eV.

4. Photocatalytic tests

We selected to work at pH 2.6 since the first acidity of carbendazim has an acidity constant K_A that yields to a $pK_A = -\log_{10}(K_A)$ equal to 4.3. In the used conditions, only positively charged organic species are expected to be present in solution. Acidic conditions in water are also supposed to help carbendazim absorption [4]. Positively charged organic molecules can indeed be absorbed easily on the negatively charged oxides nanoparticles, formed because of the light irradiation, more than on silica walls which are expected to be positively charged (because of the presence of protonated silanol groups). The used experimental conditions were chosen close those recommended for pesticides in other publications [21].

Fig. 8A displays preliminary catalytic tests that were performed with an aqueous solution containing 20 ppm of carbendazim, 2 mL of H_2O_2 (30%) and at 18 °C to limit iron leaching (a) in the dark (no visible halogen light, with CoFe₇₀₀SBA-15 catalyst) and (b) with light but without catalyst. Two straight lines were obtained. The curve labelled (c) was measured with pure calcined silica SBA-15. There was a first sharp absorption of carbendazim (concentration in solution going down, 14 ppm). Then the concentration increased and went back to 18 ppm (instead of the initial 20 ppm). Further measurements will be necessary to ascertain the origin of this wave. To avoid the pollution of further results because of possible H_2O_2 emission, we have decided to add 2 mL of pure H_2O_2 (30%) in all the other made catalytic tests, after 30 min of absorption and before opening the light. The (d) curve was obtained with Aerioxide titania P25, EVONIK® and using a UV-light for excitation. With that light, 86% of carbendazim was eliminated in 320 min.

Fig. 8B is relative to tests performed under visible light: 1) on the same titania reference, only a small reactivity was observed and an important remaining amount of carbendazim of 17.9 ppm was observed after 320 min of catalytic test, 2) 10 ppm of carbendazim were eliminated in 320 min with CoFe₇₀₀SBA-15 compared to 5 ppm only with NiFe₇₀₀SBA-15. 10 ppm of carbendazim were then absorbed and partially eliminated using 75 mg of the CoFe₇₀₀SBA-15 mixture as heterogeneous catalyst which corresponds to 133.5 mg of carbendazim by kg of catalyst.

The simple photocatalytic tests performed with the present two catalysts are interesting for fundamental reasons. A first very rapid event (initial rate between 2.79 and 0.74 ppm min⁻¹) was associated with MBC absorption and equilibration in solution. A second superimposed event was detected only after 50 min of test and was significantly slower (0.058 compared to 0.154 ppm min⁻¹). This second event was associated with the partial decomposition of the absorbed organic molecules on the catalyst surface.

Previously published results that we have obtained in similar conditions with Fe-oxides and Fe-dispersed on SBA-15 were giving up to 8–10% of the introduced Fe-species free in solution and able to act as homogeneous catalysts (Fenton, [17]). We have checked that the amount of leaching was smaller with the present CoFe₇₀₀SBA-15. No more than 2.06% of the introduced Fe-species were found in solution after 300 min of catalytic test. A small homogeneous catalytic reactivity was then involved (quantifications were performed by X-ray fluorescence during the PhD thesis of Nabil Tabaja).

To compare the activity of Aerosil titania P25 EVONIK®, NiFe₇₀₀ and CoFe₇₀₀ mixtures under sunlight, the tests (performed at 18 °C and ambient pressure) made with the three solids were reproduced and stopped after 300 min of reaction (lamp and thermostat stopped) but the solution was kept under stirring and the dark room was opened until 1400 min of reaction. The reaction continued at first under daylight for two hours (and then under the artificial light of the room for rest of the night up to 1400 min). Remaining concentrations and the degradation percentages for all the tests after 300 and 1400 min under visible light and solar light were given in Table 3. With the reference titania EVONIK®, the reaction under visible light was almost totally

stopped (no further evolution after 300 min, 17.2 ± 0.5 ppm remaining after 1400 min). With our two mixtures, CoFe₇₀₀SBA-15 and NiFe₇₀₀SBA-15, the activity was continuously increasing with time. The activity with CoFe₇₀₀ reached even 96% of carbendazim elimination but it was very slow (1400 min). The CoFe₇₀₀SBA-15 mixture was at least 3 times more active than the NiFe₇₀₀SBA-15 mixture.

A recent work was devoted to the Near-Infrared driven photocatalytic properties of lanthanide-doped NaYF₄: Er deposited on CdS core-shell nanostructures [15] and their enhanced properties was illustrated by a study of the photocatalytic elimination of carbendazim in an aqueous solution. As can be seen in Figure 10 of this publication, on the kinetical curve representing carbendazim elimination as a function of time, 40% of the initial amount of carbendazim was remaining after 6 h of reaction. 10 mg of solid catalyst were used and associated with an initial number of moles of MBC of 0.125.10⁻⁵ mole: 0.075.10⁻⁵ moles eliminated. With our CoFe₇₀₀SBA-15 mixture, we have added H_2O_2 to simplify the mechanism and used a halogen lamp that emits both in the visible and the NIR spectral range. With our best catalyst, we observed that 47% of the carbendazim remains after 6 h. We used an initial solution of 20 ppm MBC, then 0.01046 mole for 75 mg of catalyst. By dividing the initial number of moles of MBC by a factor 7.5, 1.395.10⁻⁴ moles were eliminated in our experimental conditions. The present catalyst activity was then apparently comparable to the one of the newly developed lanthanide-doped NaYF₄: Er on CdS core-shell nanostructures but the present catalysts were less expensive and less difficult to prepare.

5. Discussion about oxidation ability

Synthesis conditions giving pure CoFe₂O₄ and NiFe₂O₄ nanoparticles, with different sizes, from 2 to 50 nm and shapes spheres, nanorods and nanotubes, have been reported and tested for several oxidation reactions, as summarized in the recent review article [32]. They have also been tested for several catalytic reactions, for instance for oxygen formation and for H_2O_2 reduction [33]. For both reactions, CoFe₂O₄ has been found more active than NiFe₂O₄.

The materials described here are different, nanowires being particularly small and submitted to a very strong dispersion on the silica-support (magnetically non active) and also because of the formation of complex mixtures of several oxides. We have nevertheless observed that the CoFe₇₀₀SBA-15 mixture enriched in CoFeO₃ is more active is two times more active for a photocatalytic oxidation reaction than a NiFe₇₀₀SBA-15 mixture containing NiFe₂O₄. The two mixtures are also much more active than the reference titania Aerosil P25 EVONIK that we have selected. Comparison between the curves of photocatalytic activity obtained under a UV light excitation (Fig. 7A (d)) and a visible and NIR excitation (Fig. 7B (a)) is meaningful. Titania is a semi-conductor of large band gap and a very good photocatalyst only if a UV light is introduced, a light above 3 eV.

The explanation of the observed difference of reactivity between our mixtures containing Nickel and Cobalt is more complex and even if only nanoparticles of spinel structure are introduced, at least four factors that may affect the energy of the octahedral crystal field will have to be considered: 1) differences of electronegativities of Iron, Nickel and Cobalt ions, 2) differences of electronic configuration, all the electrons being paired with a Ni(II) ion of electronic configuration [Ar] 3d⁸ and unpaired electrons being present with a Co(II) ion, [Ar] 3d⁷, 3) strong spin-orbit couplings are expected to be present with Co (II) and absent for Ni(II) ions, 4) possible non-stoichiometries, in particular cationic or oxygen vacancies. In addition, exact percentages of cations inversion will have to be introduced and this will require more resolved diffraction data.

Despite these difficulties, we observed that the spinel unit-cell measured on NiFe₇₀₀SBA-15 was smaller than the one of CoFe₇₀₀SBA-15. Shorter Ni-O interatomic distances that Co-O distances were then involved, yielding to a larger covalence degree

Table 3

Results of carbendazim concentration measured in aqueous solution as a function of time for a reaction performed at pH 2.

| Carbendazim | | | | |
|--------------------------------|----------------------------|---------------------------|---|----------------------------|
| Sample | Remaining in 300 min (ppm) | Eliminated in 300 min (%) | Remaining after 1400 min with visible then Sun light) (ppm) | Eliminated in 1400 min (%) |
| TiO ₂ P25 Reference | 17.9 | 10.0 | 17.2 | 14 |
| NiFe ₇₀₀ _SBA-15 | 15.1 | 24.5 | 12.0 | 33.3 |
| CoFe ₇₀₀ _SBA-15 | 10.6 | 47.0 | 0.8 | 96.0 |

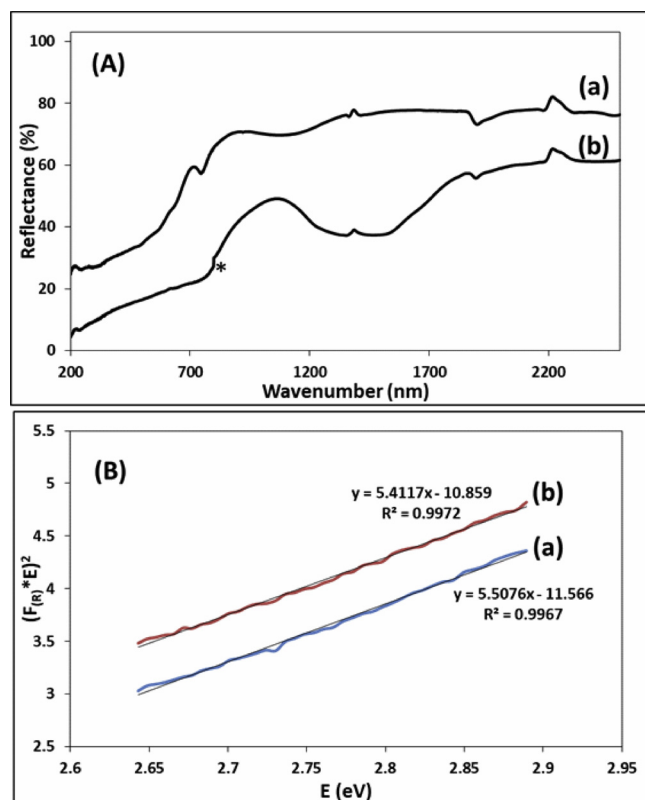


Fig. 7. A) UV-vis spectra of CoFe₇₀₀_SBA-15 (a) and NiFe₇₀₀_SBA-15 (b). The two powders have been diluted in Teflon® and spectra measured in reflectance (R%); *Artefact due to lamp change on spectrometer; Artefact (negative) at 2200 nm due to baseline correction; Bands located at 1400 and at 1900 nm corresponding mainly to water molecules absorbed on the catalyst surface. These two strong absorption at 1400 and 1900 nm are often applied for the quantification of water in bio-products, for instance in wood pellets [31]. (B) The two straight lines used to determine the third band gap value, direct, of CoFe₇₀₀_SBA-15 (2.20 eV) and NiFe₇₀₀_SBA-15 (2.09 eV).

opposed to oxygen participation to redox reactions. Despite the complex composition of the mixtures that we have studied, the observations that we have made on their photocatalytic reactivity under a visible and NIR activation agree with reported data and provide a sound basis for future investigations using more elaborated techniques and simulations (the web site of Materials Project has been contacted).

6. Conclusions and perspectives

Despite their complex composition, the mixtures of oxides that we studied were interesting because their photocatalytic reactivity under visible light is excellent. Dispersion on silica was facilitating the formation of mixtures of oxides nanoparticles, in particular CoFeO₃ in CoFe₇₀₀_SBA-15 and NiFe₂O₄ in NiFe₇₀₀_SBA-15. Measured reflectance spectra were consistent with reported data concerning films and demonstrated that our mixture were reacting with visible and NIR.

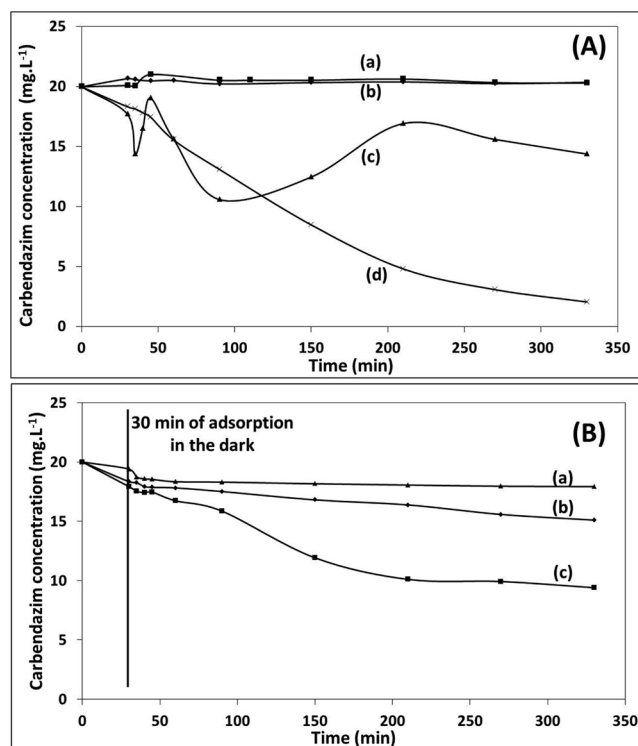


Fig. 8. Carbendazim concentration in an aqueous solution in several experimental conditions all tests being made with 2 mL of added H₂O₂ (30%): (A): (a) with a visible lamp but no catalyst (b) in the dark with CoFe₇₀₀_SBA-15; (c) with blank silica SBA₅₀₀ and (d) with a UV-lamp and TiO₂ Aerosil P25 EVONIK® (B): three tests performed under a visible lamp: (a) TiO₂ Aerosil P25 EVONIK®, (b) NiFe₇₀₀_SBA-15 and (c) CoFe₇₀₀_SBA-15.

In otherwise strictly identical experimental conditions (acidic pH, 2 mL of added H₂O₂, in air and with visible and NIR or sun activation), the activity of CoFe₇₀₀_SBA-15 was significantly larger than the one of NiFe₇₀₀_SBA-15, the two mixtures being more active than a reference Aerosil titania P25, EVONIK®.

Optimizing experimental conditions in order to obtain only nano-wires of a given M-Fe₂O₄ oxide is still an open and very interesting research subject. Using SBA-15 to stabilize dispersed nanoparticles also. Ameliorations in XRD will be obtained by using longer measurement times and by eliminating X-ray Fluorescence, using an apparatus equipped with a Mo-excitation source for instance. Recording *in situ* XANES spectra in the presence of reagents will also help us in the future for inorganic phases identification and for a better understanding of the specific properties that are associated with oxide nanoparticles when they are compared with more conventional micron-sized particles.

Acknowledgements

This work has been made in collaboration between the doctoral school of Science and Technology (T), Lebanese University and the doctoral school of Physics and Materials Chemistry (ED397), on Pierre

and Marie university campus. The work has been made in the two laboratories, Laboratory of Materials, Catalysis, Environment and Analytical Methods (MCEMA) of the Lebanese University – Beyrouth and Laboratoire de Reactivité de Surface (LRS) of Pierre and Marie Curie University – Paris.

References

- [1] Website of ECOPHYTO PRO: www.ecophyto.pro.fr.
- [2] A. Boudina, C. Emmelin, A. Baaliouamer, M.F. Grenier-Loustalot, Photochemical behaviour of carbendazim in aqueous solution, *Chemosphere* 50 (2003) 649–655.
- [3] The WHO, Recommended Classification of Pesticides by Hazard and Guidelines to Classification, International Program on Chemical Safety, IPCS, 1999.
- [4] Report of European Commission, Health and Consumers Protection Directorate-General, Directorate D. Food Safety, Unit D.3- Chemicals Contamination and Pesticides, 5 January, (2007) 5032/VI/98 final.
- [5] S. Hayar, J. Al Hadi, A. Merhi, L. Majed, L. Saba Ayon, Communication Orale, Groupe Français Des Pesticides, 18 Mai, (2017).
- [6] W.P. Wang, H. Yang, T. Xian, XPS and magnetic properties of CoFe_2O_4 nanoparticles synthesized by a polyacrylamide gel route, *Mater. Trans.* 53 (2012) 1586–1589.
- [7] M. Niederberger, N. Pinna, *Metal Oxide Nanoparticles in Organic Solvents*, Engineering Materials and Processes, Springer, Verlag London, 2009.
- [8] A.P. Alivisatos, Perspectives on the physical chemistry of semiconductor nanocrystals, *J. Phys. Chem. C* 100 (1996) 13226–13239.
- [9] C. Guibert, V. Dupuis, V. Peyre, J. Fresnais, Hyperthermia of magnetic nanoparticles: experimental study of the role of aggregation, *J. Phys. Chem. C* 119 (50) (2015) 28148–28154.
- [10] A. Sharma, A. Sharma, M. Sharma, N. Bhalla, P. Estrela, A. Jain, P. Thakur, Nanomaterial fungicides: in vitro and in vivo antimycotic activity of cobalt and nickel nanoferrites on phytopathogenic fungi, *Glob. Chall.* 1 (2017) 17–41.
- [11] N. Sanpo, C.C. Berndt, C. Wen, J. Wang, Transition metal-substituted cobalt ferrite nanoparticles for biomedical applications, *Acta Biomater.* 9 (2013) 5830–5837.
- [12] R.P. Richards, J.W. Kramer, D.B. Baker, K.A. Kriege, Pesticides in rainwater in the north-eastern United States, *Nature* 327 (1986) 129–131.
- [13] J. Rodríguez-Carvajal, Recent developments of the program FULLPROF, in commission on powder diffraction (IUCr), (<http://journals.iucr.org/iucr-top/comm/cpd/Newsletters/>). Complet. Progr. Doc. <http://www.ill.eu/sites/fullprof/26>, Newsletter 26 (2001) 12–19.
- [14] J. Tauc, *Amorphous and Liquid Semiconductor*, Plenum Press, New York, 1974, p. 159.
- [15] R. Balaji, S. Kumar, K.L. Reddy, V. Sharma, K. Bhattacharyya, V. Krishnan, Near-infrared driven photocatalytic performance of lanthanide-doped NaYF_4 @ CdS core-shell nanostructures with enhanced upconversion properties, *J. Alloys. Compd.* 724 (2017) 481–491.
- [16] Y.Y.A. Sayari, B.H. Han, Simple synthesis route to monodispersed SBA-15 silica rods, *J. Am. Chem. Soc.* 126 (2004) 14348–14349.
- [17] N. Tabaja, S. Casale, D. Brouri, A. Davidson, H. Obeid, J. Toufaily, T. Hamieh, Quantum-dots containing Fe/SBA-15 silica as “green” catalysts for the selective photocatalytic oxidation of alcohol (methanol, under visible light), *Comptes Rendus Chim.* 18 (2015) 358–367, <https://doi.org/10.1016/j.crci.2015.01.010>.
- [18] J. Van der Meer, I. Bardez-Giboire, C. Mercier, B. Revel, A. Davidson, R. Denoyel, Mechanism of metal oxide nanoparticles formation in SBA-15 silica grains, *J. Phys. Chem. C* 114 (8) (2010) 3507–3515.
- [19] C. Cornu, J.L. Bonnardet, S. Casale, A. Davidson, S. Abramson, G. Andre, F. Porcher, I. Grčić, V. Tomic, D. Vujevic, N. Koprivanac, Mechanism of metal oxide nanoparticle loading in SBA-15 by the double solvent technique, *J. Phys. Chem. C* 116 (2012) 3437–3448.
- [20] A. Davidson, J. Van der Meer, I. Bardez, F. Bart, P.A. Albouy, G. Wallez, Dispersion of Co_3O_4 nanoparticles within SBA-15 using alkane solvents, *J. Van Der Meer, I. Bardez, F. Bart, P.A. albouy, G. Wallez, A. Davidson, Microporous Mesoporous Mater.* 118 (1–3) (2009) 183–188.
- [21] F. Rouquerol, L. Lucciani, P. Llewellyn, *Techniques De l'Ingénieur*, P1050 V3, 10 Mars, (2003).
- [22] Z. Marczenko, M. Balcerzak, Ch.4. Separation, Preconcentration, Spectrophotometry in Inorganic Analysis, BOOK, 10, (2000), pp. 53–73.
- [23] A. Aziz, A. Abdul, E. Ahmed, A. Muhammad Naeem, K. Muhammad Azhar, K. Nazia, A. Irshad, Structural, electrical, dielectric and magnetic properties of Mn-Nd substituted CoFeO_3 nano sized multiferroics, *Prog. Nat. Sci.* 26 (4) (2016) 325–333.
- [24] N. Zhang, J. Brugger, B. Etschmann, Y. Ngothai, D. Zeng, Thermodynamic modeling of poorly complexing metals in concentrated electrolyte solution: an X-ray absorption and UV-vis. Spectroscopic study of Ni(II) in $\text{NiCl}_2\text{-MgCl}_2\text{-H}_2\text{O}$ system, *PLoS One* 10 (4) (2015) 0119805.
- [25] R.D. Shannon, C.T. Prewitt, Revised version of ionic radii, *Acta Cryst. B* 25 (1969) 925.
- [26] C. Lepetit, M. Che, Discussion on the coordination of Ni^{2+} ions to lattice oxygens in calcined faujasite-type zeolites followed by diffuse reflectance spectroscopy, *J. Phys. Chem.* 100 (8) (1996) 3137–3143.
- [27] J.H. Nobs, Kubelka–Munk theory and the prediction of reflectance, *Rev. Prog. Coloration Relat. Topics* 15 (1) (1985) 66–75.
- [28] R.C. Roi, S. Wilser, M. Guminiak, B. Cai, M.L. Nakarmi, Optical and electronic properties of NiFe_2O_4 and CoFe_2O_4 , *Appl. Phys. Rev.* 106 (2012) 207–211.
- [29] K.P. Reddy, R. Jain, M.K. Ghosalya, C.S. Gopinath, Metallic cobalt to spinel Co_3O_4 - electronic structure evolution by near-ambient pressure photoelectron spectroscopy, *J. Phys. Chem. C* 121 (39) (2017) 21472–21481.
- [30] B. Hoilnsworth, D. Mazumdar, H. Sims, Q.C. Sun, Chemical tuning of the optical band gap in spinel ferrites: CoFe_2O_4 versus NiFe_2O_4 , *Appl. Phys. Lett.* 103 (2013) 082406.
- [31] J. Sundaram, S. Mani, C.W.K. Kandala, R.A. Holser, Application of NIR Reflectance Spectroscopy on Rapid Determination of Moisture Content of Wood Pellets, (2015) <http://creativecommons.org/licenses/by/4.0/>.
- [32] B.I. Kharisova, H.V. Rasika Dias, O.V. Kharisova, Mini-review: ferrite nanoparticles in the catalysis, *ScienceDirect* (2019), <https://www.sciencedirect.com/science/article/pii/S1878535214002901>.
- [33] M. Li, Y. Xiong, X. Liu, X. Zhang, C. Han, L. Guo, Facile synthesis of electrospun MFe_2O_4 ($\text{M} = \text{Co}, \text{Ni}, \text{Cu}, \text{Mn}$) spinel nanofibers with excellent electrocatalytic properties for oxygen evolution and hydrogen peroxide reduction, *Nanoscience* 19 (2015) 8920–8930.